Ventilation and Transformation of Labrador Sea Water and Its Rapid Export in the Deep Labrador Current

PETER BRANDT, ANDREAS FUNK, LARS CZESCHEL, CARSTEN EDEN, AND CLAUS W. BÖNING

IFM-GEOMAR, Leibniz-Institut für Meereswissenschaften, Kiel, Germany

(Manuscript received 1 June 2005, in final form 31 July 2006)

ABSTRACT

A model of the subpolar North Atlantic Ocean is used to study different aspects of ventilation and water mass transformation during a year with moderate convection intensity in the Labrador Sea. The model realistically describes the salient features of the observed hydrographic structure and current system, including boundary currents and recirculations. *Ventilation* and *transformation* rates are defined and compared. The transformation rate of Labrador Sea Water (LSW), defined in analogy to several observational studies, is 6.3 Sv (Sv $\equiv 10^6$ m^3 s^{-1}) in the model. Using an idealized ventilation tracer, mimicking analyses based on chlorofluorocarbon inventories, an LSW ventilation rate of 10 Sv is found. Differences between both rates are particularly significant for those water masses that are partially transformed into denser water masses during winter. The main export route of the ventilated LSW is the deep Labrador Current (LC). Backward calculation of particle trajectories demonstrates that about one-half of the LSW leaving the Labrador Sea within the deep LC originates in the mixed layer during that same year. Near the offshore flank of the deep LC at about 55°W, the transformation of LSW begins in January and is at a maximum in February/March. While the export of transformed LSW out of the central Labrador Sea continues for several months, LSW generated near the boundary current is exported more rapidly, with maximum transport rates during March/April within the deep LC.

1. Introduction

The Atlantic Ocean meridional overturning circulation (MOC), composed of a northward warm water flow in the near-surface layer and a southward flow of North Atlantic Deep Water (NADW), represents an important part of the global climate system due to its associated northward heat transport. Besides the overflow regions between Greenland and Iceland, as well as between Iceland and Scotland, open ocean convection in the Labrador Sea contributes considerably to the generation of NADW. In this region, strong oceanic heat loss in winter leads to the transformation of upper NADW, the so-called Labrador Sea Water (LSW), overlying the deep waters from the overflow regions (Marshall and Schott 1999). The cyclonic circulation in the Labrador Sea, a necessary condition for deep convection associated with large late winter mixed layer depths, is composed of the West Greenland Current (WGC), the Irminger Current (IC), the Labrador Current (LC), and the North Atlantic Current (NAC) with its "Northwest Corner." The WGC imports fresh and cold water near the surface at the shelf, and the IC transports warmer and saltier water at intermediate depths into the Labrador Sea (Lazier et al. 2002). Downstream of this inflow region, the initially strong temperature maximum at intermediate depths decreases. At the shelf off Labrador at about 53°N, the southeastward deep LC is found to transport about 26 Sv (Sv $\equiv 10^6$ m^3 s^{-1}) of NADW, of which about 11 Sv are transported within the potential density range of LSW. The deep LC has a strong barotropic component and extends approximately out to the 3300-m depth contour (Fischer et al. 2004). Offshore of the deep LC, several cyclonic recirculation cells exist that are associated with an interior anticyclonic circulation around the central Labrador Sea as well as a doming of the isopycnals off the boundary current (Lavender et al. 2000). While there are different export routes of LSW out of the Labrador Sea, that is, into the Irminger Sea and to the east—even crossing the Mid-Atlantic Ridge (Sy et

Corresponding author address: Peter Brandt, IFM-GEOMAR, Leibniz-Institut für Meereswissenschaften, Düsternbrooker Weg 20, 24105 Kiel, Germany.
E-mail: pbrandt@ifm-geomar.de

DOI: 10.1175/JPO3044.1

al. 1997; Fischer and Schott 2002; Rhein et al. 2002)—the direct route along the Deep Western Boundary Current appears to represent the fastest communication between the subpolar convection region and the subtropical gyre (Schott et al. 2004).

The maximum late winter mixed layer depths in the Labrador Sea are observed offshore of the deep LC (Lavender et al. 2000). In this region, classical or deep LSW is generated during years of medium to deep convection. In addition to the classical LSW, Pickart et al. (1997, 2002) suggested that the transformation of upper LSW occurs in the western boundary current region. However, the strength of Labrador Sea convection varies strongly from year to year with deep convection in the early 1990s followed by a multiyear restratification period (Lazier et al. 2002). For the "post deep convection" period, 1996–2001, Stramma et al. (2004) as well as Kieke et al. (2006) suggested a predominant transformation of upper LSW that increasingly filled the upper levels of the central Labrador Sea.

Here, we study some basic aspects of the transformation of LSW and its export out of the Labrador Sea using an eddy-resolving numerical model of the subpolar North Atlantic. Besides identifying transformation regions and exit pathways, we want to address the relation between *ventilation* and *transformation* of LSW. While transformation is defined here as the total LSW volume change due to diapycnal fluxes, ventilation—which is associated with air–sea fluxes of trace gases—occurs when LSW is part of the mixed layer and thus in contact with the atmosphere. In general, ventilation rates and transformation rates may differ for a given potential density range.

Transformation rates, which are a controlling factor for the Atlantic MOC and meridional heat fluxes, have been estimated from observations using different datasets and/or methods: among them are air–sea fluxes of heat and freshwater (e.g., Speer and Tziperman 1992; Marsh 2000; Khatiwala et al. 2002) and inverse methods (Talley 2003; Pickart and Spall 2007). On the other hand, the increase with time of chlorofluorocarbon (CFC) inventories within a particular potential density range reflects a ventilation of this water by surface contact. Using additional assumptions regarding the equilibrium concentration with the atmosphere and the degree of CFC saturation of ventilated water, this method has also been proposed for estimating formation rates of LSW (Smethie and Fine 2001; Rhein et al. 2002; Kieke et al. 2006). However, ventilation rates are essential for the oceanic gas uptake and the global CO_2 cycle or for estimating the water mass age. Knowledge of differences between transformation and ventilation rates are therefore important when comparing results obtained using different measurement techniques.

Here, we want to address the following questions that are hard to assess from observational results: How much LSW exiting the Labrador Sea was within the mixed layer in the same year? Where and when does the water mass transformation take place, and where and when does the LSW leave the mixed layer? After describing the model, which we use to answer these questions, the methods to analyze its output fields, and the general characteristics of the model solution in section 2, the pathways of ventilated water including its subduction are analyzed by introducing an idealized ventilation tracer and by calculating backward Lagrangian drifter trajectories in section 3. In section 4, the water mass transformation is analyzed by calculating the local volume change and horizontal divergence, and by evaluating the effect of surface buoyancy fluxes. Discussion and conclusions are presented in section 5.

2. Numerical model, methods, and general characteristics

a. Model

We discuss results of a regional eddy-resolving model developed as part of the Family of Linked Atlantic Ocean Model Experiments (FLAME). The model domain covers the subpolar North Atlantic from 43° to 70°N, 71°W to 16°E. The model code is a rewritten version of the Modular Ocean Model version 2 (MOM2) Code (Pacanowski 1995) and can be found online (http://www.ifm-geomar.de/index.php?id=spflame). Primitive equations were solved on an Arakawa-B grid (Arakawa and Lamb 1977) with horizontal resolution of $^1/_{12}°$ in longitude, square grid boxes (i.e., about 5 km and thus "eddy resolving" in the Labrador Sea) and 45 vertical levels with a thickness of 10 m at the surface, increasing to 250 m at the maximum depth of 4500 m. The model setup is essentially the same as in Eden and Böning (2002) except for the following differences: the domain is reduced to the subpolar North Atlantic using open boundaries (Stevens 1991) at the northern and southern margins of the domain; harmonic diffusion and friction are replaced by isopycnal diffusion (using a diffusivity of 50 $m^2 s^{-1}$) and biharmonic friction (using a viscosity of 2×10^{10} $m^4 s^{-1}$); and the bottom boundary layer parameterization of Beckmann and Döscher (1997) is used.

Model simulations of the subpolar North Atlantic, including the one in Eden and Böning (2002), tend to be biased in their hydrographic properties; that is, they often show an ongoing salinification of the Labrador

Sea (Treguier et al. 2005). As shown in Czeschel (2004), the present model shows significantly improved hydrographic properties in comparison to previous model experiments. This is a combined effect of (i) using an open northern boundary in the Greenland Sea at 70°N, allowing for a more realistic inflow of freshwater into the subpolar North Atlantic via the East Greenland Current and outflow of saline water via the northward extension of the North Atlantic Current (Czeschel 2004), and (ii) minimizing spurious diapycnal mixing by the isopycnal mixing scheme. Note that previous models, for example, those discussed in Eden and Böning (2002) and Treguier et al. (2005), typically used a northern temperature and salinity relaxation zone instead of an open boundary formulation. In addition to the northern boundary, there is also a southern open boundary in the model along 43°N, allowing for inflow of the North Atlantic Current and outflow of the continuation of the Labrador Sea boundary current. While for the northern open boundary the barotropic inflow and outflow are prescribed (taken from a regional model simulation of the Arctic Ocean; R. Gerdes 2004, personal communication), at the southern boundary the inflow/outflow is calculated using a simple Orlanski radiation condition (Orlanski 1976; as is the baroclinic inflow/outflow in both cases). For inflow situations, temperature and salinity values are taken from a combined climatology of Levitus and Boyer (1994) and Boyer and Levitus (1997), which is also used for the initial condition.

The surface forcing is given by climatological monthly mean fields taken from a 6-hourly analysis at the European Centre for Medium-Range Weather Forecasts (ECMWF) of the years 1986–88 (Barnier et al. 1995). For the heat flux Q, the following condition is used:

$$Q = Q_0 + Q_2(\mathrm{SST}_{\mathrm{model}} - \mathrm{SST}_{\mathrm{clim}}), \qquad (1)$$

where Q_0 is the prescribed heat flux, $\mathrm{SST}_{\mathrm{model}}$ is the model sea surface temperature (SST), $\mathrm{SST}_{\mathrm{clim}}$ is the SST corresponding to surface forcing, and $Q_2 = \partial Q/\partial \mathrm{SST}|_{\mathrm{SST}_{\mathrm{clim}}}$, a function of space and time, is derived from a linearized form of the bulk formula for surface heat flux (Barnier et al. 1995). Following usual practice because of the lack of appropriate data, the freshwater fluxes are calculated by restoring sea surface salinities to Levitus data using a constant time scale of 15 days for the uppermost 10-m grid boxes. Starting from rest using Levitus climatology, the model was allowed to spin up for 10 model years while forced by the ECMWF climatology described above. Here we have analyzed a 1-yr run (model year 10) obtained with the regional model. For testing the robustness of the obtained results, specifically with respect to the eddy variability in the boundary current regime, we have for comparison also analyzed a companion 1-yr run of a basin-scale version of the $^1/_{12}°$ FLAME model that differs only in the open southern boundary shifted toward 18°S. All other aspects of both models including spinup period and northern boundary formulation are the same.

b. Methods

In the following section we describe the methods used to analyze the numerical simulation that permit a distinction between *ventilation* and *transformation* rates. Here we applied two methods to quantify ventilation rates in the model: 1) an idealized "ventilation tracer," similar to CFC, which is initialized in the mixed layer and is subject to advection and diffusion, and 2) Lagrangian drifters, which are seeded at a section across the deep LC (the main export route of LSW out of the Labrador Sea) and followed backward in time, eventually traced back to the mixed layer. The transformation rate of the model is calculated on a daily basis as the sum of local volume change and horizontal divergence for an isopycnal layer in predefined boxes. Additionally, the transformation rate exclusively due to negative surface buoyancy flux is calculated. The second method is applied to each horizontal grid cell, thereby yielding additional detailed regional distribution of this transformation rate.

1) VENTILATED LSW

The first question that we want to address is: How much of the LSW exiting the Labrador Sea was within the mixed layer during the same year? In the following, such water will be referred to as newly ventilated or simply as ventilated water. The mixed layer depth is defined using a potential density (σ_θ) criterion: water with differences in σ_θ of less than 0.01 kg m^{-3} from the surface value is defined as part of the mixed layer.

The time-varying distribution of ventilated water is investigated using an idealized dimensionless concentration C of a ventilation tracer. The evolution of the tracer concentration is calculated during the model integration. The ventilation tracer is initialized with 0 in the entire model domain at 1 January and set to a value of 1 within the mixed layer in the Labrador Sea north of 52°N and west of 43°W (see Fig. 1a) during each time step beginning at 1 January. The tracer distribution is calculated for each time step by a tracer equation including advective and diffusive terms identical to the terms used in the equations for temperature and salinity. We define the volume-integrated tracer over the entire model domain,

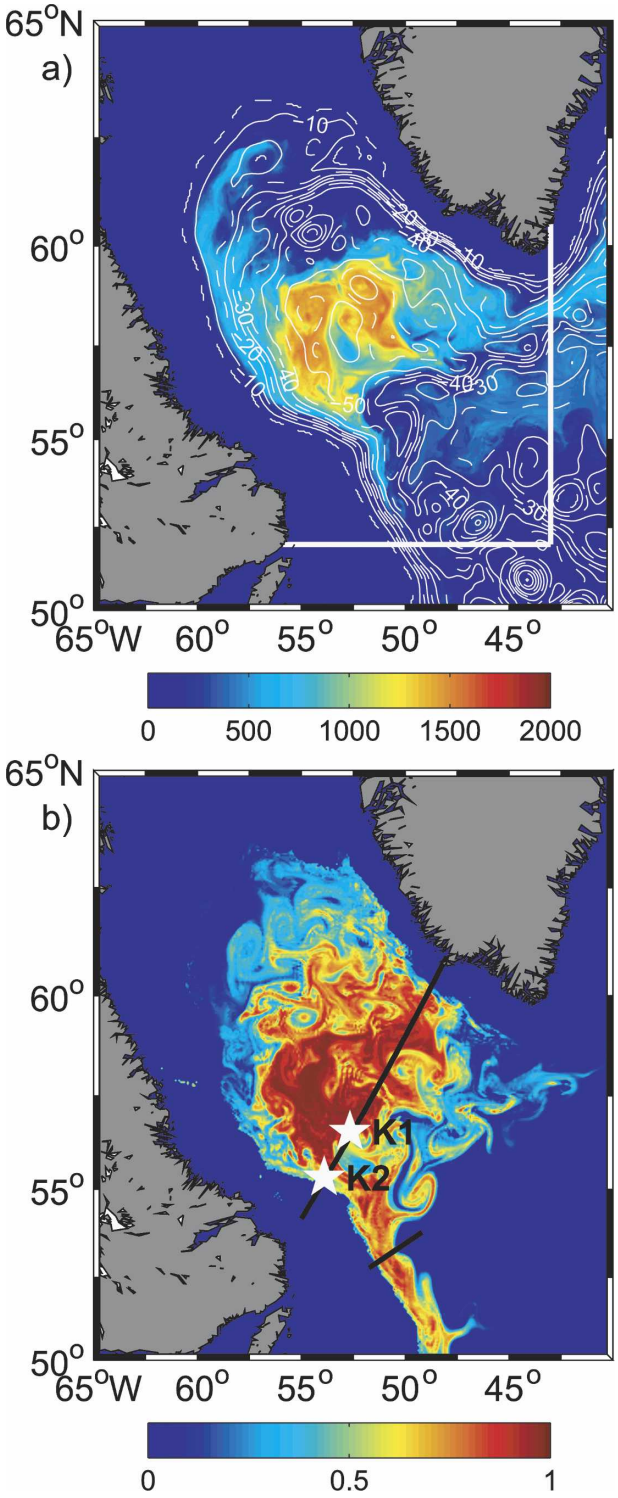

FIG. 1. (a) Simulated mixed layer depth (m; color shading) superimposed on barotropic streamfunction (Sv; isolines) during March and (b) concentration of the idealized ventilation tracer in the σ_θ range 27.77–27.80 kg m^{-3} during May; (a) also shows the chosen limits for the Labrador Sea region, i.e., the 52°N and the 43°W section, and (b) shows the LC section at about 53°N and the WOCE AR7W section running across the deep Labrador Sea, as well as the locations of moorings K1 and K2 (white stars).

$$V_C(t) = \int_V C(t)\, dV, \tag{2}$$

as the total volume of water that was ventilated in the prescribed region (north of 52°N and west of 43°W) between time $t = 0$ (1 January) and the time t.

The ventilation tracer concentration in a certain location represents a ratio of ventilated water volume to total volume; that is, for a concentration of 1 only ventilated water was present at this location and for a concentration of 0 no ventilated water reached this location. Based on this consideration, we define

$$F_A(t) = \int_A C(t)\, v_\perp(t)\, dA \tag{3}$$

as the transport of ventilated water through a section, where $v_\perp$ is the cross-section velocity component. The resulting flux can be divided into different σ_θ classes. For each σ_θ class, the section segment A is defined as that area of the section occupied by water between upper and lower bounds in σ_θ.

2) PATHWAYS OF VENTILATED LSW

The second question addresses the pathways of ventilated LSW out of the Labrador Sea. Pathways of ventilated LSW can be inferred qualitatively from the evolution of the ventilation tracer. Additionally, we apply a Lagrangian drifter method to elucidate these pathways explicitly. Drifter trajectories are calculated backward in time using daily velocity fields from the model output. The fields are interpolated in space and time, and the trajectories are calculated using a variable time step depending on local velocity. Some 100 000 Lagrangian drifters are deployed every five days at the slanted 53°N section running across the deep LC from 53°N, 52°W to 54°N, 49°W (see Fig. 1b). Each drifter is assigned a constant transport as follows: The section is divided into segments. The product of cross-section velocity component $v_{i\perp}$ and the area $A_i = \Delta x_i \times \Delta z_i$ of section segment i is the transport $M_i = A_i \times v_{i\perp}$ through that section segment. Within each section segment i, n_i drifters are distributed homogenously. Each drifter j in section segment i carries a transport $m_j = v_{j\perp} A_i / n_i$ (Döös 1995), where $v_{i\perp}$ is linearly interpolated between neighboring grid points. The numbers of drifters in different section segments are chosen such that each drifter carries approximately the same transport m_j; that is, a large (small) amount of drifters is deployed in section segments with large (small) cross-section velocities following Blanke and Raynaud (1997).

The instantaneous transport of ventilated water through the 53°N section then is the sum of all transport

values assigned to those drifters passing through the section at a given time that were found to originate in the mixed layer that same year. This transport can be directly compared to the transport calculated using Eq. (3). While the mean transport of ventilated water through the section obtained from the different methods is almost the same, both distributions differ as the ventilation tracer is affected by horizontal and vertical diffusion, while the Lagrangian drifters are not.

3) SUBDUCTION OF LSW

Once the pathways of ventilated water have been calculated, the question of where the water leaves the mixed layer can be addressed. Similar to the subduction process in the subtropics, responsible for the formation of water masses in the permanent thermocline, we define here subduction as the process in which a water particle leaves the mixed layer and is separated from air–sea fluxes. Subduction is calculated using the backward trajectories of Lagrangian drifters deployed at the 53°N section. The occurrence of subduction is identified in time and space when the respective backward trajectory enters the mixed layer. Backward drifter trajectories are calculated until the end of the year or until they reach the 50°N or 40°W section. However, only 5% of subduction occurs outside the tracer initialization area. Using this method and the deployment strategy described above, only subduction of water leaving the Labrador Sea within the deep LC is considered.

The area of the Labrador Sea is divided into horizontal grid boxes. We define an instantaneous subduction rate (on a daily basis) within a horizontal grid box as the sum of all transport values assigned to drifters subducted within this box. Note that the annual mean subduction rate, that is, the mean over the analyzed year, in the entire model domain equals the annual mean transport of ventilated water through the 53°N section as calculated from the backward trajectories.

4) WATER MASS TRANSFORMATION

The question that we want to address here is: Where does the water mass transformation take place? We will discuss two quantities: 1) an effective simulated water mass transformation that includes all effects capable of changing the water density in the model and 2) the water mass transformation due to the model's buoyancy flux that captures the essential physics of surface flux-driven convection. While the first transformation rate is evaluated for large boxes, the second one is calculated at each grid point yielding detailed information on where and when water mass transformation does occur.

Let $H(x, y, t)$ be the isopycnal layer thickness, calculated as the water column height between two given σ_θ bounds; then the following conservation equation holds:

$$\frac{\partial H}{\partial t} + \nabla_h \cdot (\overline{\mathbf{v}_h} H) = S, \tag{4}$$

where t is time, $\nabla_h \cdot$ is the horizontal divergence operator, $\overline{\mathbf{v}_h}$ is the vertically averaged horizontal velocity vector in a potential density range with thickness H, and S is a source term including effects due to surface buoyancy fluxes, diapycnal diffusion in the interior, nonlinearities in the equation of state, as well as numerical inaccuracies. We define a transformation rate T in a region that includes all the aforementioned effects by simply integrating S over the surface area of that region. Both terms on the left-hand side of Eq. (4) are calculated using daily model output fields. Annual mean volume change and horizontal divergence are calculated for different regions by integrating both terms on the left-hand side of Eq. (4) over the surface area of the regions, then averaging over time.

Assuming that the spatial mean change of isopycnal layer thickness within the entire Labrador Sea (north of 52°N and west of 43°W) during a year is zero (i.e., model in quasi-steady state), the annual mean transformation rate is given by

$$\overline{T} = \left\langle \oint \overline{v_\perp} H \, ds \right\rangle, \tag{5}$$

where $\overline{v_\perp}$ is the velocity component of $\overline{v}$ perpendicular to the line segment, ds, along the sections delimiting the Labrador Sea with an orientation westward along 52°N (southern boundary, Fig. 1a), and northward along 43°W (western boundary, Fig. 1a). The brackets in Eq. (5) represent the annual mean. The eastern and northern model boundaries of the Labrador Sea are closed. In this case the annual mean transformation rate equals the annual mean net export out of the Labrador Sea for a given σ_θ class.

In addition to the effective transformation rate determined as the sum of local volume change and horizontal divergence for a given σ_θ class, we also calculate a transformation rate from buoyancy fluxes at the ocean surface, a method originally pioneered by Speer and Tziperman (1992). Here, we apply a similar method that considers only the effect of negative surface buoyancy flux on the oceanic stratification. The buoyancy flux is defined to be negative when the resulting buoyancy of the oceanic surface layer decreases. Starting from heat and freshwater fluxes, as well as temperature and salinity profiles for each horizontal grid box, the

local transformation from lighter into denser water due to negative surface buoyancy fluxes is calculated. Here, daily model output fields are used. First, the change in temperature and salinity in the uppermost grid box due to daily heat and freshwater fluxes is calculated. The convection scheme described by Rahmstorf (1993) is applied to completely remove static instability in the water column and to obtain vertically homogeneous salinity and potential temperature profiles in the mixed layer.

After calculating σ_θ from the initial temperature and salinity profiles and the profiles obtained by applying the daily surface freshwater and heat fluxes in conjunction with the convection scheme, isopycnal layer thicknesses are calculated for initial and obtained profiles for the different σ_θ classes. The difference between the initial and obtained layer thicknesses of the respective σ_θ classes defines the daily generation/destruction of layer thickness of a particular σ_θ class due to negative surface buoyancy fluxes. The daily generated/destroyed isopycnal layer thicknesses are then summed up for different periods in time (e.g., months or seasons). The transformation rate due to negative buoyancy flux, T_{b-}, is obtained by integrating the generated/destroyed layer thicknesses of a particular σ_θ class over the surface area of the respective region and division by the time step (1 day).

While we focus only on the effect of negative buoyancy forcing, the calculation of water mass transformation presented here is similar to the approach suggested by Speer and Tziperman (1992). However, the present scheme accounts for strongly varying (and particularly large) mixed layer depths, which vary on horizontal and temporal scales of the mesoscale eddy field. This represents a first approach calculating transformation rates of LSW due to surface buoyancy fluxes in high-resolution eddy-resolving models.

c. *General characteristics of the model solution in the Labrador Sea*

In this study we focus on one 1-yr climatological simulation with the regional model described in section 2a. However, the calculations regarding the water mass transformation are repeated for another climatological simulation using the FLAME Atlantic model with an open southern boundary shifted toward 18°S with very similar results.

The climatologically forced model experiment with the regional model simulates a year of moderate convection intensity in the Labrador Sea with maximum mixed layer depths of about 1600 m in March (Fig. 1a). Similar mixed layer depths were found in the Labrador Sea for example, in 1997 (Pickart et al. 2002). More intense convection was found in particular in the early 1990s. On the other hand, significantly shallower convection depths were observed from 1998 to 2002 (Lazier et al. 2002; Stramma et al. 2004). The distribution of the idealized ventilation tracer after the convection period during May (Fig. 1b) shows that a large part of LSW in the potential density range (σ_θ = 27.77–27.80 kg m^{-3}) was part of the mixed layer in the same year. The distribution suggests that the main export route of ventilated LSW is via the deep LC.

The maximum of the annual mean overturning streamfunction as function of depth (equivalent to the vertical volume transport) calculated along the sections at 52°N, 43°W is 3.0 Sv. This value is larger than the value of 1.3 Sv reported by Böning et al. (1996). A larger vertical volume flux must be associated with a larger horizontal circulation (Spall and Pickart 2001). In fact, the maximum barotropic streamfunction in the Labrador Sea of about 55 Sv (Fig. 1a) is found to be at the upper end of those described in a model comparison study by Treguier et al. (2005), ranging from 40 to 60 Sv for different models.

With respect to many characteristics, such as flow field and distribution of eddy kinetic energy (EKE), the present model is similar to the model of Eden and Böning (2002). In their model solution as well as in the model solution presented here, a strong early winter EKE maximum within the WGC as well as a smaller late winter EKE maximum in the region of the deep LC can be found. This is in general agreement with the analysis of altimetric data (Lilly et al. 2003; Brandt et al. 2004).

Recent direct velocity measurements at the exit of the Labrador Sea show a well-defined, mainly barotropic deep boundary current and a weak recirculation farther offshore (Fischer et al. 2004, their Fig. 5). The observed structure of the Labrador Sea boundary current is, in general, well represented by the model simulations (Fig. 2). The top-to-bottom southeastward transport of the boundary current at 53°N is very similar, about 40 Sv and 38 Sv for simulated and observed boundary current transports, respectively. However, the simulated southeastward transport of LSW in the depth range σ_θ = 27.74–27.8 kg m^{-3} is 19 Sv, which is clearly above the observed value of about 11 Sv for summer 1997–99 (Fischer et al. 2004). This can partly be attributed to slightly shallower depths of simulated isopycnal surfaces. At the offshore part of this section, the potential density surface σ_θ = 27.74 kg m^{-3}, typically used to separate upper LSW from classical LSW, is observed to be at about 600 m during summer 1996 and about 900 m during summer 1999. In the model experiment presented here, the depth of this potential

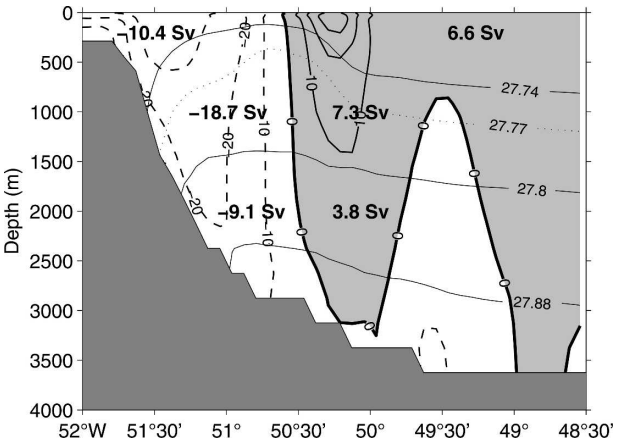

FIG. 2. July mean 53°N section of alongshore velocity (cm s^{-1}; dashed contours denote southeastward velocities, and solid contours northwestward velocities) superimposed on potential density (thin solid contours). Transport values are given for marked σ_θ layers bounded by zero isotach. The position of the slanted section is marked in Fig. 1b. The dotted line separates the two layers of LSW used in this study.

density surface is about 800 m in the offshore region with a strong isopycnal doming up to a depth of 200 m between the boundary current and the offshore recirculation (Fig. 2). Simulated doming, in excess of the observed one, is related to stronger southeastward velocities of the boundary current and stronger northwestward velocities of the recirculation in the near-surface flow, together with slightly narrower current bands. Some of these differences might be also due to the fact that the observations of Fischer et al. (2004) are taken during a period of weak convection in the Labrador Sea, while the climatological model forcing simulates convection of moderate intensity.

In most recent models, including the previous $^1/_{12}°$ FLAME version analyzed in Eden and Böning (2002), simulated LSW potential density ranges differ considerably from observed ranges (Treguier et al. 2005). This fact complicates a direct comparison of observational and modeling results with respect to the hydrographic structure of the Labrador Sea. Compared to those models, the simulated hydrographic structure of the model version at hand is substantially improved. The simulated salinity along the World Ocean Circulation Experiment AR7W section (Fig. 3a) shows a similar pattern as described by Stramma et al. (2004) and Pickart and Spall (2007). There is a deep salinity maximum at about 2000-m to 2500-m depth and increased salinities in the WGC and LC below the near-surface layer. However, the depth-averaged salinity of the present model is, although reduced compared to previous model simulations (Treguier et al. 2005), still larger than the observed salinities (Fig. 3b).

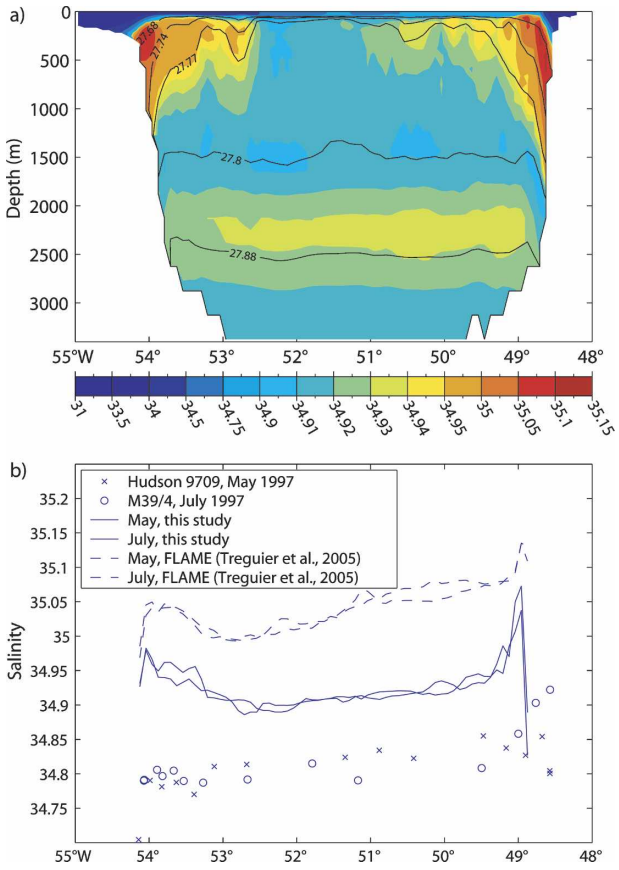

FIG. 3. (a) Simulated salinity (color shading) during June superimposed on potential density (solid lines) along the WOCE AR7W section marked in Fig. 1b. (b) Depth-averaged salinity of the upper 700 m from data collected along WOCE AR7W section in May 1997 (R/V *Hudson*) and July 1997 (R/V *Meteor*), and corresponding simulated salinities from the previous FLAME model (dashed lines) and the present model (solid lines).

The simulated and observed temporal evolution of the temperature field at the two mooring positions K1 and K2 marked in Fig. 1b are shown for the period January to May (Fig. 4). The observational data correspond to the year 1997. While the simulated temperature in the boundary current in particular is larger than observations indicate (note the different color scales in Fig. 4), the structure of the temporal variability at the two positions agrees quite well. At mooring position K1, representing the central Labrador Sea regime, a continuous deepening of the mixed layer is observed only disturbed by single eddy events. Note that the mixed layer deepening is slightly faster in the model compared to the data. At mooring position K2, representing the boundary current regime, a strongly variable temperature field is found as the result of an intense eddy field advected along the boundary current in both simulation and observation, while the mean wintertime cooling of the upper 500-m boundary cur-

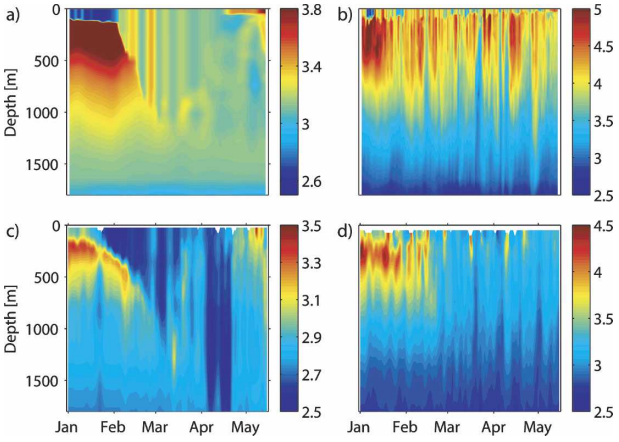

FIG. 4. Evolution of (a), (b) simulated and (c), (d) observed potential temperature (°C) at mooring positions (a), (c) K1 and (b), (d) K2 marked in Fig. 1b. The observations are from 1997. Note the different temperature scales.

rent waters is weaker in the model compared to the data.

We conclude that the simulated flow field and hydrographic structure are within or close to observed ranges. In the following, we apply different methods to identify pathways of ventilated water masses as well as to calculate ventilation and transformation rates. The water mass definition for LSW is chosen as the isopycnal range $\sigma_\theta = 27.74$–27.80 kg m^{-3}, similar to that used in observational studies (e.g., Fischer et al. 2004). We will further separate the LSW layer into an upper layer defined by $\sigma_\theta = 27.74$–27.77 kg m^{-3} and a lower layer defined by $\sigma_\theta = 27.77$–27.80 kg m^{-3} (cf. Fig. 2 and Fig. 3a).

3. Pathways of ventilated water masses

The export of ventilated water within the depth range of LSW mainly occurs in the deep LC. Only a minor contribution to the total export of ventilated LSW leaves the Labrador Sea across the 43°W section. This is illustrated in the May concentration of the ventilation tracer within the isopycnal range $\sigma_\theta = 27.77$–27.80 kg m^{-3} showing high tracer concentration up to 0.8 in the deep LC and low tracer concentration east of 43°W (Fig. 1b). In the following we will investigate this main export route of LSW using backward Lagrangian drifter trajectories.

By calculating Lagrangian trajectories of drifters deployed at the 53°N section in the deep LC backward in time until 1 January using daily velocity fields, we confirm that a large part of the total southeastward transport of LSW leaving the Labrador Sea at 53°N originates in the mixed layer that same year. The distribution of ventilated water at the 53°N section is illustrated by the ratio of annual mean ventilated water transport

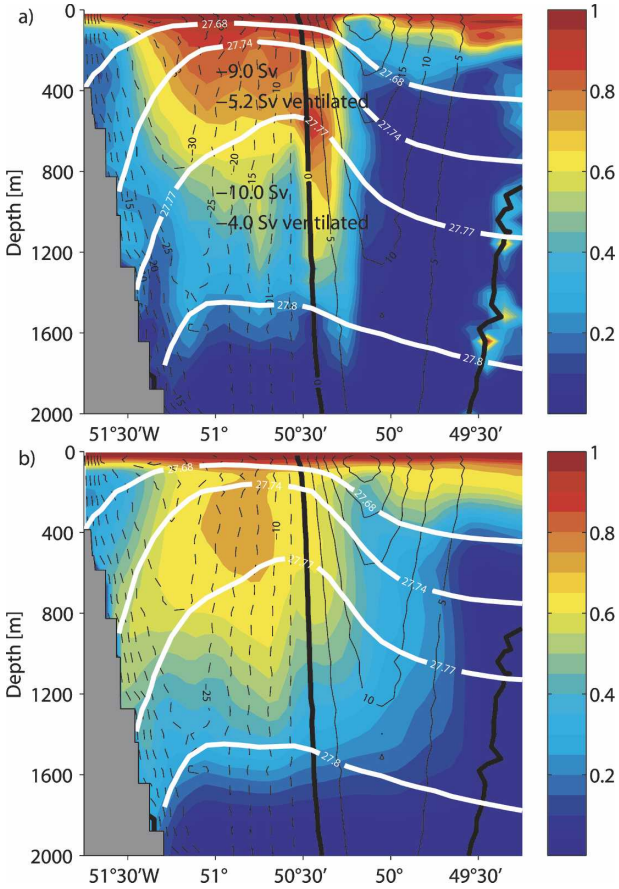

FIG. 5. Ratio of annual mean ventilated water transport to annual mean transport at the 53°N section marked in Fig. 1b (color shading) as obtained (a) from backward Lagrangian drifter trajectories and (b) from the idealized ventilation tracer. Also included are annual mean alongshore velocities (cm s^{-1}; black contours, where dashed contours denote negative velocities, solid contours are positive velocities, and thick solid contours are zero velocity) and selected isopycnal depths, σ_θ (kg m^{-3}; thick white contours). Transport values in (a) are given for annual mean transport and annual mean transport of ventilated water for selected σ_θ layers bounded by the zero isotach.

(sum of transport values assigned to drifters that originate in the mixed layer) to annual mean transport for each section segment. Owing to the small number of drifters, the ratio is not well defined for very small cross-sectional velocities (Fig. 5a).

The annual mean relative contribution of such ventilated LSW to the southeastward transport of LSW at 53°N is about 60% for the upper LSW layer and about 40% for the lower LSW layer (Fig. 5a). The distribution of the ventilation tracer at the 53°N section (Fig. 5b) shows a pattern similar to the distribution of ventilated water from the Lagrangian drifter calculations. The main differences are the smoother shape and slightly broader pattern in the case of the ventilation tracer.

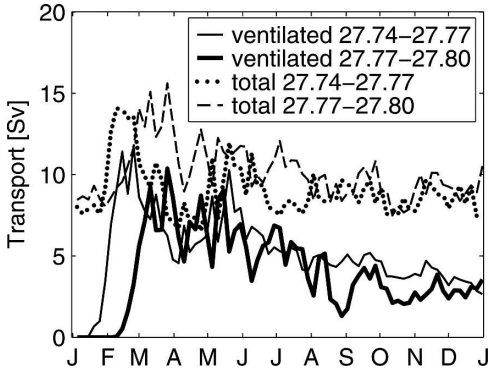

FIG. 6. Time series of southeastward LSW transport and ventilated LSW transport across the slanted 53°N section (see Fig. 1b) for different σ_θ classes as obtained from backward Lagrangian drifter trajectories.

These differences are attributed to the fact that the distribution of the ventilation tracer is subject to vertical and horizontal diffusion, while the Lagrangian pathways are purely obtained from advection using daily velocity fields.

The southeastward transport of LSW at 53°N has a seasonal transport maximum in February/March. Ventilated LSW as obtained from Lagrangian drifter calculations is exported out of the Labrador Sea beginning in February within the upper LSW layer and in March within the lower LSW layer (Fig. 6). The large transport values in winter demonstrate a rapid export of newly ventilated LSW along the western boundary pathway, starting as early as the convection period. The relative contribution of ventilated LSW shows a near-steady decrease after the early export peak with a slight secondary maximum in May. At the end of the year, about 30% of the southeastward LSW export still consists of LSW that was part of the mixed layer during that same year.

From the backward drifter trajectories the subduction rate of LSW is calculated as explained in section 2b. The subduction rate is divided into different σ_θ classes according to the σ_θ value of the drifter at the 53°N section. The subduction velocity (Fig. 7a) is calculated by dividing the subduction rate of each horizontal grid cell by its surface area. The largest annual mean subduction velocities are found in the region around 56°N, 56°W within the deep LC. The time series of the subduction rate within Box 1 shows that at this location subduction starts early in the year with a total maximum in March/April (Fig. 7b).

4. Water mass transformation

In the model, the mean wintertime buoyancy fluxes are characterized by strong buoyancy losses in the central Labrador Sea (Fig. 8). The buoyancy flux is calculated using the heat flux defined by Eq. (1) (see section 2a) and the freshwater flux resulting from the restoring of sea surface salinities to Levitus data. In general, there is a stronger buoyancy loss over the deep LC relative to the central Labrador Sea. This is associated with strong air–sea temperature differences over the deep LC, particularly due to the upward mixing of heat originating from the IC that imports relatively warm and salty waters at intermediate depths into the Labrador Sea. In the WGC, mostly anticyclonic eddies are generated, which are capped by a layer of cold and less salty coastal waters. The shedding of these eddies results in a reduction of the buoyancy flux along the eddy migration pathways into the interior Labrador

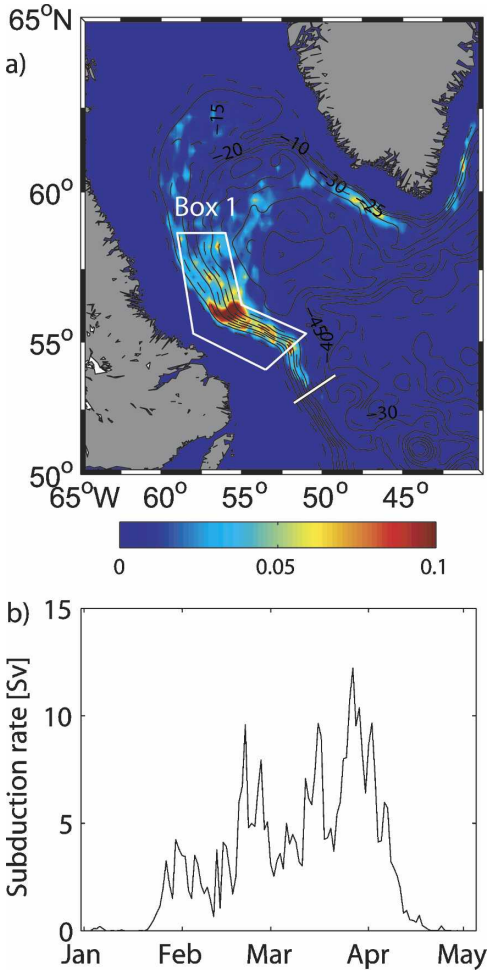

FIG. 7. Subduction of LSW (σ_θ = 27.74–27.80 kg m^{-3}) leaving the Labrador Sea within the deep LC across the 53°N section (thick white solid line) as obtained from backward Lagrangian drifter trajectories: (a) spatial pattern of subduction velocity (mm s^{-1}; color shading) overlaid on annual mean barotropic streamfunction (Sv; black contours) and (b) time series of subduction rate in box 1 marked in (a).

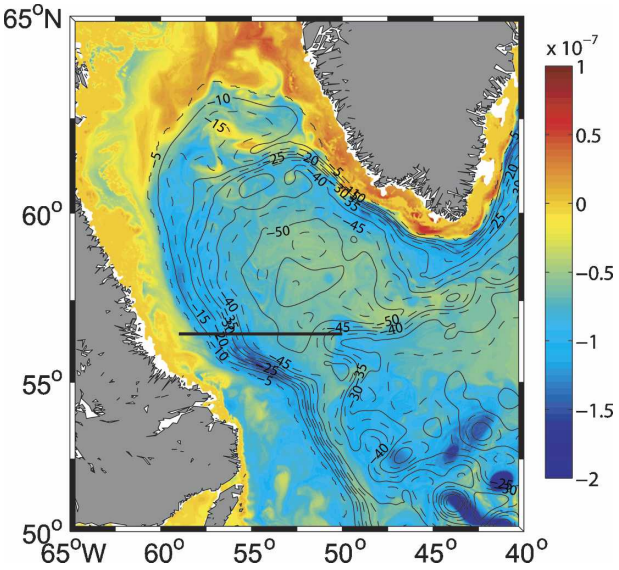

FIG. 8. Mean January–April buoyancy flux ($m^2\ s^{-3}$; color shading) superimposed on mean January–April barotropic streamfunction (Sv; black contours). Also shown is the 56.5°N section crossing the LC and central Labrador Sea (thick solid line).

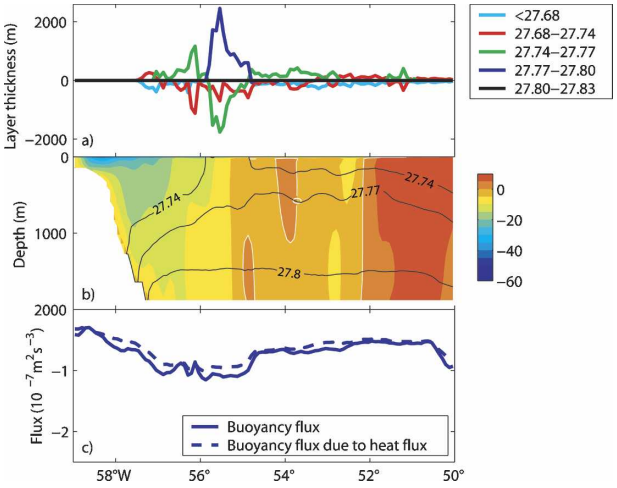

FIG. 9. January (a) thickness changes of isopycnal layers defined by given σ_θ-bounds due to negative surface buoyancy flux, (b) mean meridional velocity (cm s^{-1}; color shading, white contours denote zero velocity) overlaid on potential density (black contours), and (c) total buoyancy flux (solid line) and buoyancy flux due to heat flux only (dashed line). All quantities are plotted along 56.5°N marked in Fig. 8.

Sea. Note that these relatively small-scale variations of the buoyancy flux (Fig. 8) are generated by the difference between simulated SST and climatological values [Eq. (1)]. A comparison between satellite SST and model simulation (Emery et al. 2006) reveals in general good agreement, in particular with respect to variations in the boundary currents. However, it is difficult to assess the realism of the buoyancy flux since there is clearly a lack of surface flux data acquired during winter capable of resolving the high temporal and spatial variability in the area.

In the following, we will discuss the water mass transformation along a zonal section at 56.5°N, chosen for its location directly north of the main subduction region. The surface buoyancy forcing is dominated by the buoyancy flux due to surface heat flux, and the freshwater flux contributes less than 10% to the total forcing in general (Figs. 9 and 10). The water mass transformation, presented here as a change of isopycnal layer thickness, commences in January with the transformation of water with σ_θ = 27.68–27.77 kg m^{-3} into water with σ_θ = 27.77–27.80 kg m^{-3}. This early transformation occurs in the transition region between the boundary current and interior Labrador Sea. Here, the stratification is considerably weaker compared to the strongly stratified shallow LC farther onshore (Fig. 9b). Within this region, the buoyancy loss is at its maximum and a slight doming of the isopycnals (in particular σ_θ = 27.74 kg m^{-3}) is observed. Large values of generated layer thicknesses, in some areas much larger than the layer thickness of a particular potential density class, can only be obtained by a rapid export of the transformed water masses. Thus, this transformation has to occur in a region where the deep LC transports water southeastward out of the Labrador Sea (Fig. 9). At the same time, lighter and particularly warmer water masses are continuously imported into the region of water mass transformation.

During March, the water mass transformation area becomes broader and reaches farther east (Fig. 10).

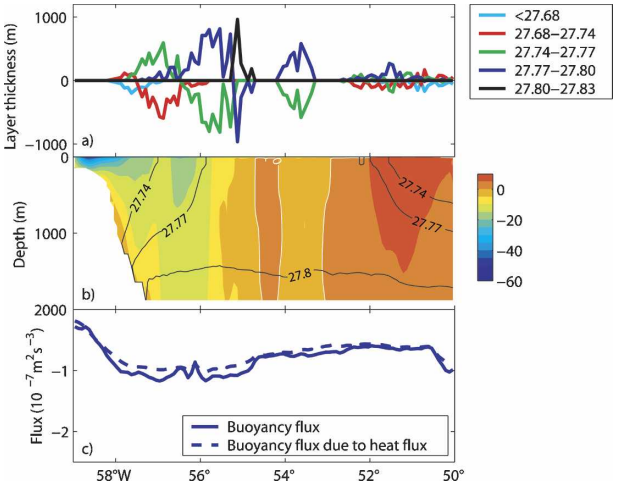

FIG. 10. As in Fig. 9 but for March.

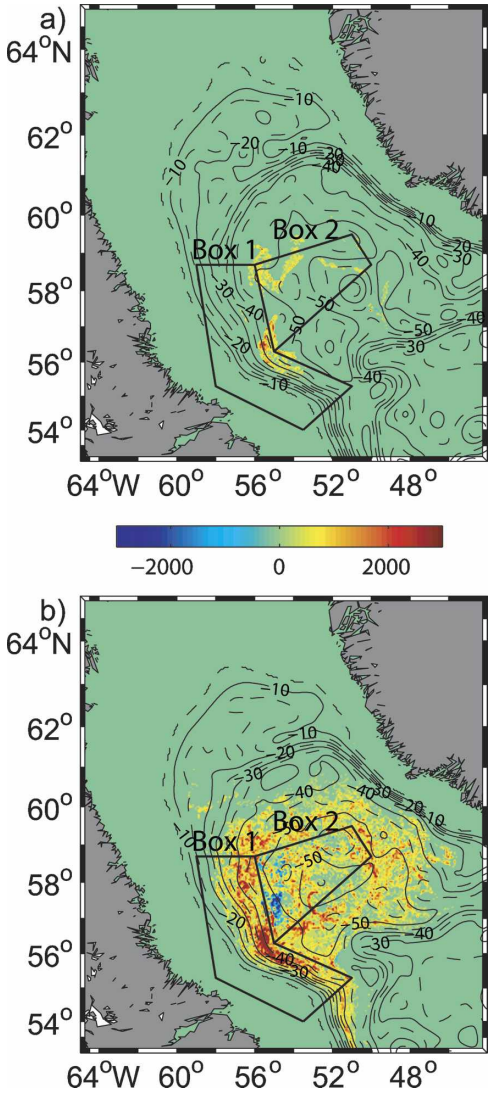

FIG. 11. (a) January and (b) January–March thickness changes (m) of isopycnal layer σ_θ = 27.77–27.80 kg m^{-3} due to negative surface buoyancy flux (color shading) superimposed on barotropic streamfunction (Sv: black contours). Also included are box 1 and box 2 representing the near–boundary current regime and central Labrador Sea regime, respectively.

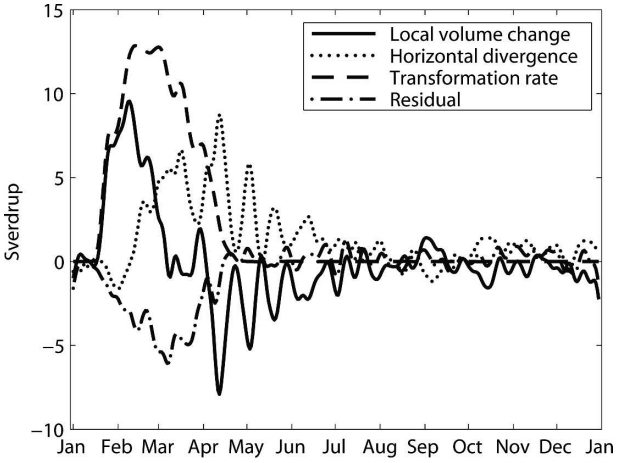

FIG. 12. Time series (10-day low-passed) of local volume change (solid line), horizontal divergence (dotted line), transformation rate due to negative surface buoyancy flux (dashed line), and residual (dashed–dotted line) within box 1 marked in Fig. 11 for σ_θ = 27.77–27.80 kg m^{-3}.

However, strongest transformation rates are obtained at the offshore flank of the deep LC. The regional distribution of simulated water mass transformation indicates the early start of water mass generation with σ_θ = 27.77–27.80 kg m^{-3} predominantly in the southern part of the Labrador Sea at about 55°W near the deep LC (Fig. 11a). During the first three months of the year within the southern part of the Labrador Sea, more than 3000–m layer thickness of water with σ_θ = 27.77–27.80 kg m^{-3} is generated locally. In the central Labrador Sea, negative transformation rates indicate a destruction of layer thickness of water with σ_θ = 27.77–27.80 kg m^{-3} associated with the transformation of denser water masses (Fig. 11b).

For two boxes, as well as for the entire Labrador Sea, the transformation rates due to negative buoyancy flux are compared to the local volume change and horizontal divergence [see section 2b, Eqs. (4) and (5)]. While Box 1 represents the near–boundary current regime of the deep LC, Box 2 represents the central Labrador Sea regime with deepest mixed layer depths during winter (Fig. 11). The residual marked in Figs. 12 and 13 is then the sum of the local volume change and horizontal divergence (effective transformation rate) minus the transformation rate due to negative buoyancy flux. This residual accounts for other transformation rates, that is, due to positive surface fluxes, diapycnal diffusion, nonlinearities in the equation of state, as well as numerical inaccuracies. In particular, this residual may be due to the assumption made for the calculation of the transformation rate due to negative buoyancy flux; that is, the buoyancy fluxes act on a given stratification for a whole day, neglecting in this way effects of lateral/vertical advection/diffusion in the model capable of changing the stratification during a day. The annual means of local volume change, horizontal divergence, and transformation rate due to negative buoyancy flux (Sv) for the three regions and different isopycnal layers are given in Table 1, where the sum of the first two columns of each region represents the effective annual mean transformation rate of the model. Positive values in Table 1 are associated with the volume increase of a potential density class in the respective region. Note that the annual-mean local volume change for all po-

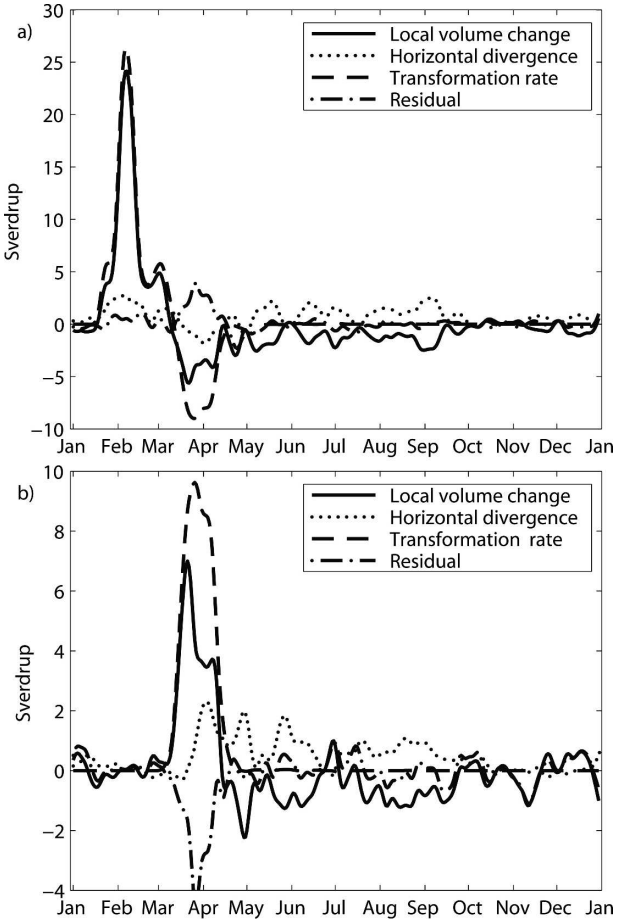

FIG. 13. As in Fig. 12 but for Box 2 marked in Fig. 12; (a) σ_θ = 27.77–27.80 kg m^{-3} and (b) σ_θ = 27.80–27.83 kg m^{-3}.

tential density classes is rather small, indicating that the model is approximately in a quasi-steady state (Table 1).

From the annual-mean transformation rates due to negative buoyancy flux (Table 1), we conclude that about one-third of the LSW transformation for σ_θ = 27.77–27.80 kg m^{-3} occurs in Box 1, while about two-thirds of LSW transformation is spread over large parts of the Labrador Sea (Fig. 11b). In Box 2, the annual mean transformation rates are smaller, but denser water masses (σ_θ = 27.80–27.83 kg m^{-3}) are also generated here. From the horizontal divergence, we find a net inflow into Box 1 of water with potential density of $\sigma_\theta < 27.74$ kg m^{-3} and a net outflow of water with σ_θ = 27.74–27.80 kg m^{-3}, while for Box 2, we find a net inflow of water with $\sigma_\theta < 27.77$ kg m^{-3} and correspondingly a net outflow of water with σ_θ = 27.77–27.83 kg m^{-3}.

The temporal evolution of local volume change, horizontal divergence, and transformation rate due to negative buoyancy fluxes for the isopycnal layer σ_θ = 27.77–27.83 kg m^{-3} of Box 1 indicates that the transformation starts in mid-January and leads initially to a local volume change of that isopycnal layer (Fig. 12). The export of this water mass out of Box 1, which is represented by the horizontal divergence, starts at the beginning of February with maximum values in March/April. The export rapidly decreases with the end of negative buoyancy fluxes and associated water mass transformation in mid-April (Fig. 12).

In the central Labrador Sea (Box 2) the negative buoyancy fluxes lead to the generation of water with σ_θ = 27.77–27.80 kg m^{-3} from the end of January to the beginning of February, and directly results in an increase of the simulated volume of that isopycnal layer (Fig. 13a). Throughout the year, the horizontal divergence is weak, nevertheless yielding an almost continuous export out of Box 2 between May and October. During March/April, negative transformation rates are obtained that are associated with the generation of denser water masses. Similarly, these denser water masses (σ_θ = 27.80–27.83 kg m^{-3}) are continuously exported out of Box 2 between May and October (Fig. 13b). In summary, strongest water mass transformation rates are obtained in the near–boundary current box (Box 1). The export out of this box is already at a maximum during the convection period, indicating a rapid exit pathway of transformed water masses within the deep LC. The export of transformed water masses from the central Labrador Sea (Box 2) is a slow process, continuing over several months. We have checked the robustness of the obtained results by analyzing also a different eddy-resolving model realization based on the last year of a 10-yr spinup of a basin-scale version of the FLAME model. The comparison between both model realizations shows that the distribution of the transformation rate is very similar (cf. Fig. 11b and Fig. 14). This similarity applies consequently to Figs. 8–13. It suggests that in climatological simulations the internal year-to-year variability of the annual mean transformation rate is small.

5. Summary and discussion

Ventilation, transformation, and export of LSW have been investigated using a numerical simulation performed with an eddy-resolving model of the subpolar North Atlantic with climatological forcing. The model realistically describes some salient features of the circulation in the subpolar North Atlantic: most of the analyzed model characteristics fall within or are close to the range of observed characteristics. The chosen model experiment represents a year of moderate con-

TABLE 1. Annual-mean local volume change, horizontal divergence, and water mass transformation rate due to negative surface buoyancy fluxes for different σ_θ classes for the entire Labrador Sea limited by the 52°N and the 43°W sections (Fig. 1a), the near-boundary current region (Box 1), and the central Labrador Sea (Box 2, see Fig. 11): Units are Sverdrups.

	Labrador Sea			Box 1			Box 2		
σ_θ class	Local volume change	Horizontal divergence	Transformation rate	Local volume change	Horizontal divergence	Transformation rate	Local volume change	Horizontal divergence	Transformation rate
<27.68	−0.2	−3.3	−4.7	0.0	−0.1	−0.5	0.0	−0.1	−0.2
27.68–27.74	0.2	−3.1	−3.9	0.0	−1.5	−1.8	−0.1	−0.4	−0.4
27.74–27.77	0.0	1.2	1.5	0.0	0.2	0.2	−0.1	−0.7	−0.7
27.77–27.80	0.1	5.0	6.4	0.1	1.4	2.1	0.1	0.7	0.7
27.80–27.83	−0.2	0.6	0.7	0.0	−0.1	0.0	0.1	0.5	0.7
>27.83	0.1	−0.4	0.0	0.0	0.1	0.0	−0.1	0.1	0.0

vection intensity with March mixed layer depths of about 1600 m.

We distinguish between transformation rate and ventilation rate. The effective transformation rate of the model is calculated as the sum of local volume change and horizontal divergence for a given isopycnal layer, Eq. (4). Additionally, the transformation rate due to negative surface buoyancy fluxes is calculated based on a method originally proposed by Speer and Tziperman (1992). It is found that LSW is predominantly transformed at the offshore flank of the deep LC.

The ventilation rate is calculated by applying two methods: 1) an idealized ventilation tracer and 2) backward Lagrangian drifter trajectories. Both methods are used to describe the temporal evolution and export pathways of newly ventilated LSW. The main export route of ventilated LSW in the present model simulation is the deep LC (Fig. 1b). From backward drifter calculations, we find that about 50%, or 9.2 Sv, of LSW leaving the Labrador Sea at 53°N within the deep LC originates in the mixed layer that same year (Fig. 5a). The subduction of mixed layer water leaving the Labrador Sea within the deep LC is found to occur mainly in the southern part of the Labrador Sea during the convection period (Fig. 7).

By evaluating Eq. (4), we find in the near-boundary current box a maximum volume change for the lower part of LSW ($27.77 < \sigma_\theta < 27.80$ kg m^{-3}) in early February. The maximum volume change coincides with the onset of strong LSW transformation as inferred from negative buoyancy fluxes. The LSW transformation peaks in February/March (Fig. 12). The simulated early start of LSW transformation within the near–boundary current region agrees well with recent findings of an observational study by Cuny et al. (2005), who have done a detailed analysis of heat fluxes and mixed layer depths in the Labrador Sea based on observed CTD profiles and moored stations. Using early winter density profiles and applying air–sea heat fluxes, they derived mixed layer depths in late winter/early spring and compared them with the observed profiles. Starting with a profile at the position of mooring B1244 in the deep LC (see Fig. 14 for its location), they were not able to simulate any significant mixed layer deepening. Starting with a profile that is advected cyclonically around the Labrador Sea, from the northern Labrador Sea to the position of mooring B1244, they obtained good agreement between simulated and observed profiles, confirming the importance of water mass transformation along the deep LC pathway as suggested in Figs. 11b and 14.

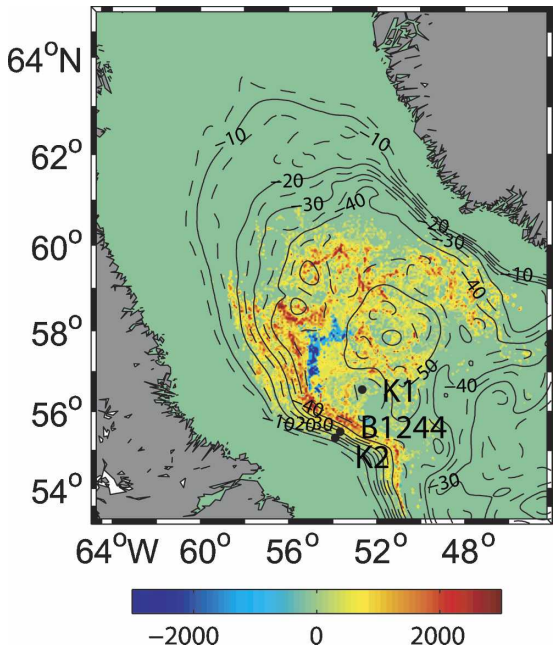

FIG. 14. January–March thickness changes (m) of isopycnal layer $\sigma_\theta = 27.77$–27.80 kg m^{-3} due to negative surface buoyancy flux (color shading) superimposed on barotropic streamfunction (Sv: black contours) for the FLAME Atlantic model. Also included are mooring positions K2, B1244, and K1.

When interpreting hydrographic sections, mainly taken during summer, it is important to know how quickly transformed water is flushed out of the Labrador Sea and what is the seasonal cycle of the transformed water export. In our model analysis we find that the export of transformed LSW out of the near-boundary current box (given by its horizontal divergence) undergoes a strong seasonal cycle, with maximum export rates in February/March and high values until May (Fig. 12). Accordingly, the analysis of backward Lagrangian trajectories yields maximum southeastward export of newly ventilated LSW across the 53°N section at about the same time (Fig. 6). Both analyses suggest a rapid export of transformed/ventilated LSW out of the Labrador Sea made possible due to the proximity of the main water mass transformation region to the deep LC. In contrast, water masses transformed in the central Labrador Sea are exported more slowly (Fig. 13).

The picture drawn by the model appears consistent with the recent analysis of observational data by Pickart et al. (2002). They suggested two types of water mass products: 1) the classical "gyre product" transformed seaward of the deep LC and 2) a "boundary product" transformed in the deep LC approximately near the 2500-m depth contour where the alongshore velocity is $O(10\ \mathrm{cm\ s^{-1}})$. The dynamical role of the boundary current in water mass transformation, hardly to be estimated from data alone, was studied by Spall (2004) using a model of an idealized marginal sea. He found a main temperature balance in the model boundary current between the warming due to mean advection and cooling due to surface heat loss and lateral eddy fluxes. The resulting downwelling in his model is located within a narrow boundary layer over the sloping bottom and at the offshore flank of the boundary current. The present model, while principally in agreement with that distribution, refines this picture by allowing inferences about the transformation and ventilation patterns in a realistic Labrador Sea setting.

The differences between transformation and ventilation rates, defined by Eqs. (5) and (3), can clearly be seen by accumulating annual mean isopycnal transport and isopycnal transport of ventilated water along the 52°N and 43°W sections limiting the Labrador Sea (Fig. 15). There is a net annual mean inflow into the Labrador Sea of lighter water ($\sigma_\theta < 27.74\ \mathrm{kg\ m^{-3}}$) of 6.4 Sv and of denser overflow waters ($\sigma_\theta > 27.83\ \mathrm{kg\ m^{-3}}$) of 0.4 Sv. Water within the potential density range $27.74 < \sigma_\theta < 27.83\ \mathrm{kg\ m^{-3}}$ is net exported out of the Labrador Sea, yielding a transformation rate of 6.8 Sv (Fig. 15a). Ventilated water is exported out of the Labrador Sea in all potential density classes with $\sigma_\theta < 27.83\ \mathrm{kg\ m^{-3}}$. As discussed before, besides the main export of ventilated LSW in the deep LC, there is only a minor contribution to the total export of ventilated LSW by the export across the 43°W section (Fig. 15b).

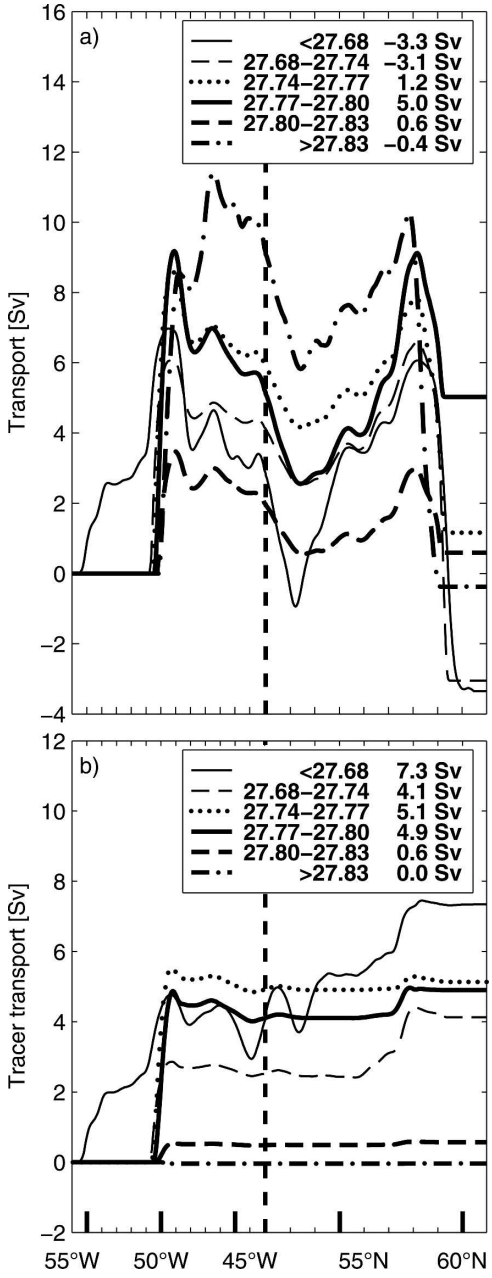

FIG. 15. (a) Annual mean cross-sectional transport and (b) annual mean cross-sectional transport of ventilated water for different σ_θ classes accumulated along the sections at 52°N and 43°W marked in Fig. 1a, starting at the coast of Labrador at 52°N, 56°W. The straight vertical dashed lines mark the corner at 52°N, 43°W. Also given in (a) and (b) are annual mean transformation rates, $\overline{T}$ [Eq. (5)], and annual mean ventilation rates, $\overline{F_A}$ [Eq. (3)], in the Labrador Sea for different σ_θ classes, respectively.

The annual mean export rate of ventilated LSW of about 10 Sv is larger than the annual mean transformation rate of LSW (6.3 Sv) calculated as the sum of local volume change and horizontal divergence (Table 1). This means that the exported LSW contains more water that originates in the mixed layer that same year than was generated by water mass transformation. While we find good agreement between ventilation and transformation rates for the higher potential density classes $\sigma_\theta = 27.77$–27.83 kg m^{-3} (giving some confidence in the chosen mixed layer criterion), for all lighter density classes, in particular for upper LSW ($\sigma_\theta = 27.74$–27.77 kg m^{-3}), ventilation rates are larger than transformation rates (cf. Fig. 15a and 15b).

To understand this apparent contradiction, consider a case of zero water mass transformation. In such a case the amount of water mass generated is the same as the amount of water mass destroyed. Although there is no change in volume, part of the water mass could have been in contact with the atmosphere and, thus, ventilated accordingly. Therefore differences between transformation and ventilation rates are present, in particular for those water masses that are partially transformed into denser water masses during winter. This holds also for long-term averages. This result is important for the analysis of CFC inventories, an observational tool for ventilation rates. Our results suggest, for example, that during years of classical LSW generation, transformation rates of upper LSW derived from CFC measurements would be overestimated.

Last, caveats regarding a possible overestimate of the near-boundary current effects in the model are related to the structure of the boundary current. In fact, the simulated boundary current appears stronger than observed, and proximity of the boundary current and recirculation results in a stronger doming of isopycnals in between than observed (Fischer et al. 2004). In addition the simulated boundary current is associated with slightly warmer and saltier waters at intermediate depths than observations indicate. However, there is a large year-to-year variability in the hydrographic structure of the boundary current, and the obtained results can be seen as an exemplary case describing the different processes relevant for the ventilation, transformation, and export of LSW during a specific year.

Acknowledgments. This work was supported by the German Science Foundation (DFG) as part of the ''Sonderforschungsbereich'' SFB 460 ''Dynamics of Thermohaline Circulation Variability.'' We thank F. Schott, J. Fischer, and M. Dengler for helpful discussions. The authors acknowledge the model development efforts of the Kiel FLAME group that provided the basis for the present simulations. The model integrations were performed at the German Climate Computing Centre (DKRZ), Hamburg, Germany.

REFERENCES

Arakawa, A., and V. R. Lamb, 1977: Computational design of the basic dynamical processes of the UCLA general circulation model. *Methods Comput. Phys.,* **17,** 173–265.

Barnier, B., L. Siefridt, and P. Marchesiello, 1995: Thermal forcing for a global ocean circulation model using a three-year climatology of ECMWF analyses. *J. Mar. Syst.,* **6,** 363–380.

Beckmann, A., and R. Döscher, 1997: A method for improved representation of dense water spreading over topography in geopotential-coordinate models. *J. Phys. Oceanogr.,* **27,** 581–591.

Blanke, B., and S. Raynaud, 1997: Kinematics of the Pacific equatorial undercurrent: An Eulerian and Lagrangian approach from GCM results. *J. Phys. Oceanogr.,* **27,** 1038–1053.

Böning, C. W., F. O. Bryan, W. R. Holland, and R. Döscher, 1996: Deep-water formation and meridional overturning in a high-resolution model of the North Atlantic. *J. Phys. Oceanogr.,* **26,** 1142–1164.

Boyer, T. P., and S. Levitus, 1997: *Objective Analysis of Temperature and Salinity for the World Ocean on a ¼ Degree Grid.* NOAA Atlas NESDIS 11, 62 pp.

Brandt, P., F. A. Schott, A. Funk, and C. S. Martins, 2004: Seasonal to interannual variability of the eddy field in the Labrador Sea from satellite altimetry. *J. Geophys. Res.,* **109,** C02028, doi:10.1029/2002JC001551.

Cuny, J., P. B. Rhines, F. Schott, and J. Lazier, 2005: Convection above the Labrador continental slope. *J. Phys. Oceanogr.,* **35,** 489–511.

Czeschel, L., 2004: The role of eddies for the deep water formation in the Labrador Sea. Ph.D. thesis, Leibniz-Institut für Meereswissenschaften an der Universität Kiel, 95 pp.

Döös, K., 1995: Interocean exchange of water masses. *J. Geophys. Res.,* **100,** 13 499–13 514.

Eden, C., and C. Böning, 2002: Sources of eddy kinetic energy in the Labrador Sea. *J. Phys. Oceanogr.,* **32,** 3346–3363.

Emery, W. J., P. Brandt, A. Funk, and C. Böning, 2006: A comparison of sea surface temperatures from microwave remote sensing of the Labrador Sea with in situ measurements and model simulations. *J. Geophys. Res.,* **111,** C12013, doi:10.1029/2006JC003578.

Fischer, J., and F. A. Schott, 2002: Labrador Sea Water tracked by profiling floats—From the boundary current into the open North Atlantic. *J. Phys. Oceanogr.,* **32,** 573–584.

——, ——, and M. Dengler, 2004: Boundary circulation at the exit of the Labrador Sea. *J. Phys. Oceanogr.,* **34,** 1548–1570.

Khatiwala, S., P. Schlosser, and M. Visbeck, 2002: Rates and mechanisms of water mass transformation in the Labrador Sea as inferred from tracer observations. *J. Phys. Oceanogr.,* **32,** 666–686.

Kieke, D., M. Rhein, L. Stramma, W. M. Smethie, D. A. LeBel, and W. Zenk, 2006: Changes in the CFC inventories and formation rates of upper Labrador sea water, 1997–2001. *J. Phys. Oceanogr.,* **36,** 64–86.

Lavender, K. L., R. E. Davis, and W. B. Owens, 2000: Mid-depth

recirculation observed in the interior Labrador and Irminger Seas by direct velocity measurements. *Nature,* **407,** 66–69.

Lazier, J. R. N., R. Hendry, A. Clarke, I. Yashayaev, and P. Rhines, 2002: Convection and restratification in the Labrador Sea, 1990–2000. *Deep-Sea Res.,* **49A,** 1819–1835.

Levitus, S., and T. P. Boyer, 1994: *Temperature.* Vol. 4, *World Ocean Atlas 1994,* NOAA Atlas NESDIS 4, 117 pp.

Lilly, J. M., P. B. Rhines, F. Schott, K. Lavender, J. Lazier, U. Send, and E. d'Asaro, 2003: Observations of the Labrador Sea eddy field. *Progress in Oceanography,* Vol. 59, Pergamon Press, 75–176.

Marsh, R., 2000: Recent variability of the North Atlantic thermohaline circulation inferred from surface heat and freshwater fluxes. *J. Climate,* **13,** 3239–3260.

Marshall, J., and F. Schott, 1999: Open-ocean convection: Observations, theory, and models. *Rev. Geophys.,* **37,** 1–64.

Orlanski, I., 1976: A simple boundary condition for unbounded hyperbolic flows. *J. Comput. Phys.,* **21,** 251–269.

Pacanowski, R. C., 1995: MOM 2 documentation: Users and reference manual. GFDL Ocean Group Tech. Rep. 3, 232 pp.

Pickart, R. S., and M. A. Spall, 2007: Impact of Labrador Sea convection on the North Atlantic meridional overturning circulation. *J. Phys. Oceanogr.,* in press.

——, ——, and J. R. N. Lazier, 1997: Mid-depth ventilation in the western boundary current system of the sub-polar gyre. *Deep-Sea Res.,* **44,** 1025–1054.

——, D. J. Torres, and R. A. Clarke, 2002: Hydrography of the Labrador Sea during active convection. *J. Phys. Oceanogr.,* **32,** 428–457.

Rahmstorf, S., 1993: A fast and complete convection scheme for ocean models. *Ocean Modell.,* **101,** 9–11.

Rhein, M., J. Fischer, W. M. Smethie, D. Smythe-Wright, C. Mertens, D.-H. Min, U. Fleischmann, and A. Putzka, 2002: Labrador Sea Water: Pathways, CFC inventory, and formation rates. *J. Phys. Oceanogr.,* **32,** 648–665.

Schott, F. A., R. Zantopp, L. Stramma, M. Dengler, J. Fischer, and M. Wibaux, 2004: Circulation and deep-water export at the western exit of the subpolar North Atlantic. *J. Phys. Oceanogr.,* **34,** 817–843.

Smethie, W. M., and R. A. Fine, 2001: Rates of North Atlantic deep water formation calculated from chlorofluorocarbon inventories. *Deep-Sea Res.,* **48,** 189–215.

Spall, M. A., 2004: Boundary currents and watermass transformation in marginal seas. *J. Phys. Oceanogr.,* **34,** 1197–1213.

——, and R. S. Pickart, 2001: Where does dense water sink? A subpolar gyre example. *J. Phys. Oceanogr.,* **31,** 810–826.

Speer, K., and E. Tziperman, 1992: Rates of water mass formation in the North Atlantic Ocean. *J. Phys. Oceanogr.,* **22,** 93–104.

Stevens, D. P., 1991: The open boundary condition in the United Kingdom Fine-Resolution Antarctic Model. *J. Phys. Oceanogr.,* **21,** 1494–1499.

Stramma, L., D. Kieke, M. Rhein, F. A. Schott, I. Yashayaev, and K. P. Koltermann, 2004: Recent deep water changes at the western boundary of the subpolar North Atlantic. *Deep-Sea Res.,* **51,** 1033–1056.

Sy, A., M. Rhein, J. Lazier, K. P. Koltermann, J. Meincke, A. Putzka, and M. Bersch, 1997: Surprisingly rapid spreading of newly formed intermediate waters across the North Atlantic Ocean. *Nature,* **386,** 675–679.

Talley, L. D., 2003: Shallow, intermediate, and deep overturning components of the global heat budget. *J. Phys. Oceanogr.,* **33,** 530–560.

Treguier, A. M., S. Theetten, E. P. Chassignet, T. Penduff, R. Smith, L. Talley, J. O. Beismann, and C. Böning, 2005: The North Atlantic subpolar gyre in four high-resolution models. *J. Phys. Oceanogr.,* **35,** 757–774.